PAPER

A general and scalable approach to produce nanoporous alloy nanowires with rugged ligaments for enhanced electrocatalysis†

H.-J. Qiu, [ID] ‡*[a] J. J. Gao,‡[a] F.-K. Chiang,‡[b] Y. R. Wen,*[c] A. Y. Yao,[d] P. Du,[a] G. Fang,[a] J. Q. Wang*[d] and X. J. Liu [ID] *[ae]

Nanoporous metal nanowires with large surface areas, and a high density of defect sites play an important role in catalysis. Here, a general and scalable one-step dealloying strategy is developed to prepare nanoporous alloy nanowires with controllable compositions by manipulating the grain size, structure and composition of bulk Cu-based precursor alloys. We prepared PtCuAu nanoporous nanowires with a diameter of 200–500 nm and tunable composition by dealloying a diluted $Pt_1Au_{0.5}Cu_{98.5}$ single-phase alloy with nanoscale column-like-structured grains. Material characterization suggests that the formation of separated nanowires is due to the large-scale shrinkage of the column-structured grains during dealloying of Cu, which also generates ultrafine nanopores and rugged alloy ligaments with a high density of defect sites in the nanowires. When used as a cathodic catalyst for the oxygen reduction reaction (ORR), the PtCuAu nanoporous nanowires exhibit a composition-dependent catalytic performance. The 8.0 M HNO_3 dealloyed sample exhibits a specific activity of 4.12 mA cm^{-2} at 0.9 V, which is more than 14 times that of commercial Pt/C. With the advantages of being easy to scale up, highly reproducible and controllable, the fabrication strategy holds great promise to prepare nanocatalysts for fuel cells.

1. Introduction

As green and sustainable energy conversion devices, room temperature fuel cells have received wide interest. However, the practical application of fuel cells is greatly hindered by the low reaction kinetics of the oxygen reduction reaction (ORR). It is well known that platinum is the most active metal for the ORR.[1–12] However, the stability of the Pt nanocatalyst is far from satisfactory.[13] To enhance the catalytic durability, Pt has been alloyed with different metals or combined with different supports. For example, Pt alloyed with non-noble metals such as Fe, Co, Ni, Cu, *etc.* has shown enhanced catalytic activity and durability with lower cost.[14–24] However, the slow dissolution of non-noble metals under electrochemical working conditions would still decrease the performance. Recently, it was found that the addition of a small amount of noble metal Au would greatly stabilize Pt or Pt-based alloy catalysts. The stabilization effect of Au on Pt can be attributed to charge transfer, electronic effects, the enhanced oxidation potential of Pt and the decoration of Pt surface defect sites such as steps.[26] Doping a small amount of Au also hinders the dissolution of transition metals such as Cu from PtCu alloy nanoparticles.[25,26] Density functional theory (DFT) calculations further show that electron transfer from Pt to Au combined with strain and ensemble effects would result in a synergistic promotion of the ORR on a Pt–Au surface.[27–29] On the other hand, to overcome the problem of sluggish ORR kinetics, Pt-based nanomaterials with various shapes and structures have been prepared, such as nanoplates,[22] nanocubes,[30] nanoframes,[31–35] nanowires,[36–38] and so on.[39–44] Among all these nanostructures, one-dimensional nanowires have drawn much attention due to their unique catalytic and electrochemical properties.[45,46] For example, the high aspect ratio of nanowires usually contributes to higher specific surface areas and potentially boosts the number of active sites at the interface.[38]

To fabricate Pt-based nanowires, many strategies have been developed, such as solvothermal reduction using *N,N*-dimethylmethanamide as solution, electrodeposition using anodic aluminum oxides (AAO) as templates, galvanic replacement reaction using Ag nanowires or Te nanowires as templates,

[a]School of Materials Science and Engineering, Harbin Institute of Technology, Shenzhen, 518055, China. E-mail: qiuhuajun@hit.edu.cn; lxj@xmu.edu.cn

[b]National Institute of Clean-and-Low-Carbon Energy, Beijing 102209, China

[c]School of Materials Science and Engineering, University of Science and Technology Beijing, Beijing 100083, China. E-mail: wyrcsu@163.com

[d]Ningbo Institute of Materials Technology and Engineering, Chinese Academy of Sciences, Ningbo 315201, China. E-mail: jqwang@nimte.ac.cn

[e]State Key Laboratory of Advanced Welding and Joining, Harbin Institute of Technology, Shenzhen 518055, China

† Electronic supplementary information (ESI) available. See DOI: 10.1039/c8ta03544j

‡ These authors are co-first authors.

This journal is © The Royal Society of Chemistry 2018

J. Mater. Chem. A, 2018, **6**, 12541–12550 | 12541

electrospinning, $etc.$[47–52] However, these methods usually involve tedious preparation steps, the use of organic solutions, $etc.$ Moreover, the composition and geometry of these Pt based nanocatalysts are difficult to control simultaneously by these bottom-up approaches. Therefore, further developing a facile and scalable fabrication strategy is greatly needed to fill the gap between laboratory research and practical application.

In recent years, dealloying has been demonstrated to be a scalable top-down strategy to prepare bulk nanoporous metals by dealloying bulk alloys or nanoporous nanoparticles by dealloying alloy nanoparticles.[53–58] Compared with bulk nanoporous metals, nanoporous nanoparticles do possess some advantages in catalysis, such as enhanced surface areas/active sites and easier mass transfer.[56] However, large-scale synthesis of an alloy nanoparticle precursor that is suitable for dealloying is still difficult. It will be very fascinating and important if one can prepare uniform nanoporous nanoparticles such as nanoporous nanowires or nanospheres on a large scale through one-step dealloying bulk alloy precursors. Theoretically, if we can manipulate the grain size in a bulk precursor alloy down to the nanoscale, and these connected grains can be separated from each other by physical or chemical means after dealloying, nanoporous nanoparticles can also be prepared by dealloying bulk precursor alloys. However, in most bulk precursor alloys, the grain size is several tens of micrometers[59] and these grains are well-connected with each other after dealloying. Thus, fabricating separated nanoporous nanoparticles by dealloying bulk precursor alloys has not been reported yet. In this work, by manipulating the grain size, grain structure and grain volume shrinkage of diluted Cu-based precursor alloys, we developed a general, scalable and straightforward dealloying strategy to prepare uniform and well-separated nanoporous nanowires with tunable composition. To demonstrate this concept, nanoporous PtCuAu nanowires with a diameter of ~200–500 nm and inherent rugged ligaments have been prepared by dealloying a designed $Cu_{98.5}$–$Au_{0.5}$–$Pt_{1.0}$ precursor alloy. The elemental composition and ratio in the nanoporous nanowires can be easily controlled by adjusting the precursor alloy composition or dealloying conditions. Owing to the structure advantage and composition control, these novel nanoporous alloy nanowires with rugged alloy ligaments, and a high density of defect sites show much superior electrocatalytic performance towards the ORR when compared with commercial Pt/C nanoparticulate catalysts.

2. Results and discussion

Energy-dispersive X-ray spectrometry (EDS) analysis in Fig. S1a (ESI†) suggests that the precursor alloy composition is in good agreement with the designed ratio ($Cu_{98.5}Au_{0.5}Pt_{1.0}$). The X-ray diffraction (XRD, Fig. 1) pattern of the precursor shows three diffraction peaks, which can be assigned to the (111), (200), and (220) diffractions of a face-centered-cubic (FCC) phase. The positions of three peaks match well with those of pure Cu, suggesting that the doped Pt and Au should distribute uniformly in the bulk Cu crystal and such a low level doping does not affect the XRD peak positions of Cu. Compared with
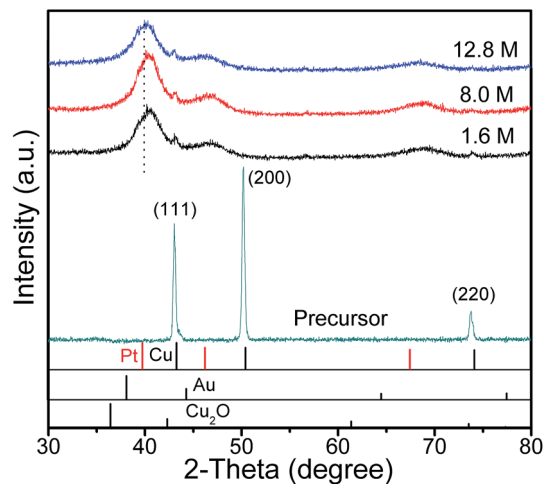

Fig. 1 XRD patterns of the precursor alloy before and after dealloying in 1.6 M, 8.0 M and 12.8 M HNO$_3$ solutions. The standard positions of Pt (JCPDS 65-2868), Cu (JCPDS 04-0836), Au (JCPDS 04-0836) and Cu$_2$O (JCPDS 05-0667) are included for comparison.

the standard diffraction patterns of Cu, the (200) peak of the precursor is much stronger, suggesting most grains align along the [200] orientation. After the dealloying, the brown precursor alloy turns black, indicating the dealloying of Cu. The XRD patterns of the dealloyed samples (Fig. 1) show that three new broad diffraction peaks located at around 41.2, 47.7, and 70.7° (2θ) appear, which can be ascribed to the (111), (200) and (220) diffractions of an FCC structure. The broad peaks may imply the formation of a nanoscale structure. Compared with that of the sample dealloyed in 12.8 M HNO$_3$, the (111) peaks of the samples dealloyed in 8.0 M and 1.6 M HNO$_3$ shift slightly to the right, suggesting that more Cu is left in these two samples. This result is also in good agreement with EDS measurements which show that the Cu content is around 27, 37, and 45 at% for the sample dealloyed in 12.8 M, 8.0 M and 1.6 M HNO$_3$, respectively (Fig. S1b–d†). The small XRD peaks at around 41.9° should be due to the existence of some Cu$_2$O when the residual Cu comes into contact with air.

EBSD analysis shows that by optimizing the melt-spinning parameters such as spinning rate and pressure, we can effectively decrease the grain diameter to 1–4 µm (Fig. S2†). Similar colors of these grains indicate their similar crystal orientation, which is in accordance with XRD results. After dealloying, the top-view scanning electron microscopy (SEM) image (Fig. 2a) shows that these well-connected grains become separated islands filled by micro-scale vacancy channels and their size decreases to ~200–500 nm. The section view SEM image (Fig. 2b) shows that these separated islands are actually the end sections of aligned nanowires with a length of ~20 µm. From the section-view image and some single nanowires (denoted by arrows), we can see that the diameter at one end is clearly larger than that of the other end, which may be caused by a large temperature gradient across the thickness of the alloy ribbons when they were produced on the cold Cu wheel. The end that is in contact with the Cu wheel has a smaller diameter due to the fast cooling. These nanowires are very weakly connected and
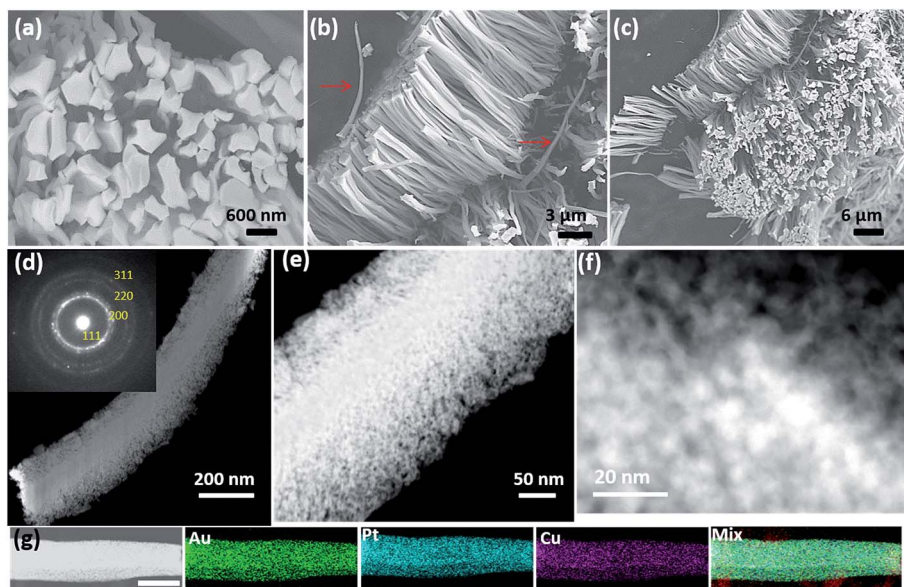
12542 | J. Mater. Chem. A, 2018, 6, 12541–12550

This journal is © The Royal Society of Chemistry 2018

Fig. 2 SEM images of the sample dealloyed in 8.0 M HNO$_3$: plane-view image (a); section-view image (b); a zoom-out image showing the large scale of nanowires (c). Dark field STEM ((d) low magnification and (e) high magnification), and high-angle annular dark field STEM (f) images of the nanoporous nanowires. EDS mapping of a single nanowire (g). Inset in (d) is the corresponding SAED image (from inside to outside is 111, 200, 220, 311). Scale bar is 250 nm in (g).

they can be easily separated as a suspension by a mild sonication treatment. A zoom-out image in Fig. 2c shows the high yield and uniformity of these nanowires. Scanning transmission electron microscopy (STEM) images (Fig. 2d) further show a single nanowire of ~200 nm in diameter and one end is slightly wider than the other, which is in agreement with the SEM observation. The nanowires exhibit an inherent nanoporous structure with uniformly distributed bright metallic ligaments and dark nanopores of ~2–4 nm across the whole nanowire (Fig. 2e). The selected area electron diffraction (SAED) pattern (inset in Fig. 2d) and the atomic resolution high-angle annular dark-field (HAADF) STEM image (Fig. 3) indicate the polycrystalline nature of the nano-ligaments. It is also observed from Fig. 2f, 7c and d that the alloy ligaments are quite uneven with many small nanoholes and very thin edges as indicated by the brightness difference in the nanoscale ligaments, which is clearly different from traditionally dealloyed nanoporous metals with smooth ligaments. From the zoom-in STEM image (Fig. 3), (111) lattice planes with a measured distance of ~0.21 nm dominate on the alloy ligaments and the (111) plane is rich in low coordinated atoms such as steps and kinks. Fig. 3b and its inset further show that the exposed (111) surface is very rough and contains many (111) steps and terraces. From the surface plots of Fig. 3a and b (i.e., Fig. 3c and d), besides the terraces from the center to the outer surface, uneven contrast of atom columns was found near the ligament surface, where some parts are very thin and some are thicker. The rugged ligament surface would clearly increase the number of step-edge sites and under-coordinated atoms, which are active for catalytic reactions such as the CO oxidation reaction and oxygen reduction reaction as observed using an environmental STEM[60] and a scanning tunneling microscope (STM),[61] respectively.

Fig. 2g shows the EDS mapping of a single nanoporous nanowire. We can see that the three main elements are distributed uniformly across the whole nanowire. It is worth mentioning that the samples dealloyed in 1.6 M and 12.8 M HNO$_3$ show quite similar morphologies and nanoporous structures to that dealloyed in 8.0 M.

The formation of well-separated nanowires is clearly owing to the large-scale volume shrinkage of each column-like-structured grain in the precursor alloy. Since the length of the nanowires is quite close to the thickness of the alloy ribbons, the lateral shrinkage vertical to the ⟨100⟩ direction clearly dominates during the dealloying process. Based on the final composition of the nanowire, the removal of Cu is over 96 at% of all atoms. Thus, the total volume shrinkage plus the nanopores generated inside the nanowires would account for over 96% of the original volume of the precursor alloy if we do not consider the size difference of Pt, Cu, and Au atoms. The large scale and fast removal of Cu may also be responsible for the formed rugged ligaments with a high density of defect sites, considering that these noble metal atoms have to travel a much longer distance to form continuous nano-ligaments. Alternatively, this low content of noble metals can only protect a certain amount of Cu and nanoholes in ligaments have to form to compensate for the vacancies caused by the large-scale removal of Cu. It is worth mentioning that changing Pt and Au to other noble metals such as Rh, Ru, or Ir does not affect the grain structure of the highly diluted Cu-based alloys. Thus, this strategy can be used to fabricate different Cu-based nanoporous alloy nanowires. The corresponding results will be reported in further work.

X-ray photoelectron spectroscopy (XPS) shows that the nanowires mainly contain Cu, Pt, and Au (Fig. 4a). The two Pt 4f
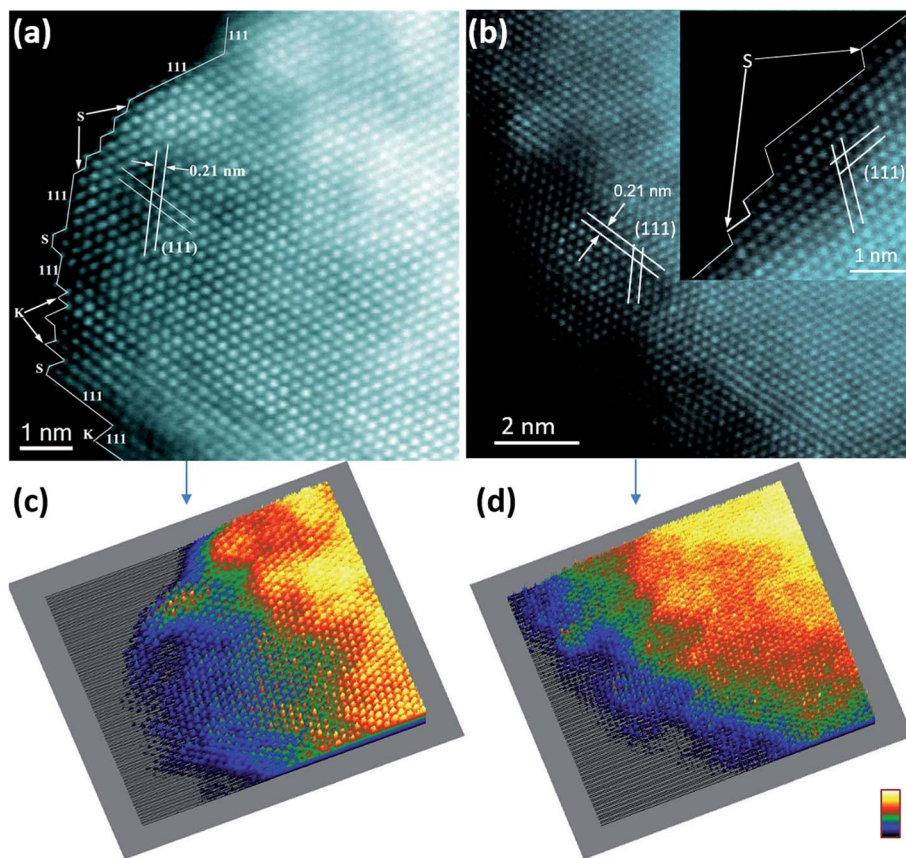
Fig. 3 HAADF STEM images (a and b) and corresponding surface plots (c and d) with false color of the alloy ligaments of nanoporous nanowires. Low-coordinated steps and kinks are denoted as S and K, respectively. (111) planes dominate in the alloy ligaments. Very thin edge can be found in (b).

peaks are located at 71.0 and 74.5 eV, which can be assigned to the Pt $4f_{7/2}$ and Pt $4f_{5/2}$, respectively (Fig. 4b). Each peak can be further split into two doublets, associated with Pt^0 and Pt^{2+} chemical states. The result suggests the existence of PtO or $Pt(OH)_2$ on the surface. Compared with that of Pt/C (71.3 eV), the Pt^0 $4f_{7/2}$ binding energy of the PtCuAu nanowires shifts
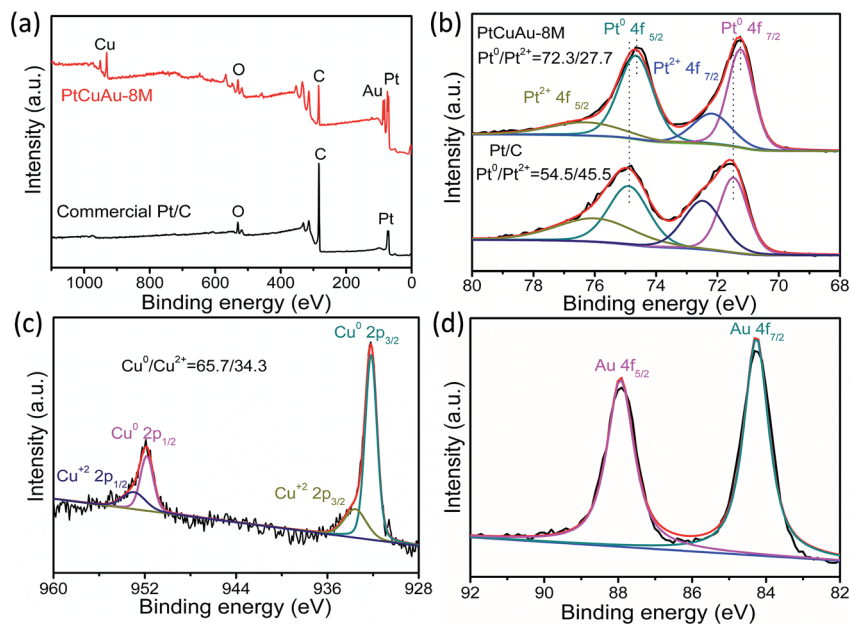

Fig. 4 XPS spectra of scan (a), Pt 4f (b), Cu 2p (c) and Au 4f (d) of the nanoporous PtCuAu nanowires dealloyed in 8 M HNO_3. The XPS scan spectrum and Pt 4f of commercial Pt/C are included in (a) and (b), respectively, for comparison.

12544 | *J. Mater. Chem. A*, 2018, **6**, 12541–12550

This journal is © The Royal Society of Chemistry 2018

negatively, indicating the change in the electronic structure due to the charge transfer between these elements or surface strain effect. The ratio of Pt^0/Pt^{2+} in the nanoporous nanowire (72.3 : 27.7) is larger than that in the Pt/C (54.5 : 45.5). It has been reported that the high ratio of Pt^0 can provide more free Pt sites for the catalytic reaction, thus enhancing the catalytic activity.[62] The Cu 2p spectrum (Fig. 4c) shows that, whilst most Cu is in the form of Cu^0 (932.4 eV), a weak signal from Cu^{II} (935.0 eV) also exists. The presence of a small amount of Cu^{II} can be due to the diffusion of Cu to the surface and its oxidation by air. Due to the high chemical stability, Au is mainly in the metallic state. The Au 4f spectrum in Fig. 4d shows two peaks at 84.2 eV and 87.8 eV, which can be ascribed to the Au $4f_{7/2}$ and Au $4f_{5/2}$, respectively, of Au^0. The XPS results of the other two nanoporous nanowire samples, which are very similar to that of the 8 M dealloyed one, are shown in Fig. S3.† The N_2 adsorption–desorption isotherms in Fig. S4† suggest the mesoporous structure of the nanowires with a Brunauer–Emmett–Teller (BET) surface area of $\sim$21 $m^2 g^{-1}$. The detected nanopore size is $\sim$4 nm which is in rough agreement with the SEM result.

The PtCuAu nanoporous nanowires with three different Cu contents were studied as a cathode catalyst for the ORR. Based on the dealloying solution concentrations, they are named as PtCuAu-12.8 M, PtCuAu-8 M, and PtCuAu-1.6 M, respectively. Fig. 6(a1–d1) show cyclic voltammetry (CV) curves of the three nanowires and commercial Pt/C in 0.1 M $HClO_4$ electrolyte. They all show characteristic CV curves of Pt. The peaks between 0 V and 0.3 V are from the hydrogen adsorption/desorption. Between 0.3 V and 0.5 V is the double-layer area. The surface begins to be oxidized when the potential is over 0.5 V and reduced during the backward scan. When compared with that of Pt/C, the reduction peaks of surface oxides on all the PtCuAu catalysts shift to a higher potential (denoted by the dotted line), indicating a weaker interaction between PtCuAu and

oxygenated species, which was often observed in highly active ORR catalysts. Based on the hydrogen adsorption charge, the EASA of the PtCuAu-8M is determined to be $\sim$51 $m^2 g^{-1}$, comparable with that of the commercial Pt/C ($\sim$60 $m^2 g^{-1}$).

Fig. 5a shows the ORR polarization curves of the four catalysts in 0.1 M $HClO_4$ aqueous solution saturated with O_2. For all the catalysts, two distinguishable potential regions can be observed, i.e., the mixed kinetic-diffusion controlled region from $\sim$0.75 to 1.0 V and the well-defined diffusion controlled region between 0.2 and $\sim$0.7 V with a diffusion-limited current density of $\sim$6 mA cm^{-2}. Both the onset and half-wave potentials of the nanoporous nanowires are clearly more positive than that of Pt/C. For example, the 8.0 M HNO_3 dealloyed sample (PtCuAu-8 M) shows a half-wave potential of $\sim$0.92 V vs. RHE, more than 80 mV higher than that of Pt/C, suggesting the much enhanced ORR activity of the nanoporous ternary nanowires. To accurately compare the intrinsic activities toward the ORR, both EASA and Pt mass normalized Tafel curves are plotted in Fig. 5b and c, respectively. It can be seen that all the nanoporous nanowire samples exhibit greatly improved specific and mass activities compared with those of Pt/C in the whole potential range (0.86–0.94 V vs. RHE). The PtCuAu-8 M sample exhibits the highest EASA specific activity of 4.12 mA cm^{-2} at 0.9 V, which is more than 14 times that of Pt/C (0.28 mA cm^{-2}) measured under the same conditions. PtCuAu-8 M also delivers a high mass activity of 1.45 A mg$_{Pt}^{-1}$, which is $\sim$6.6 times that of Pt/C (0.22 A mg$_{Pt}^{-1}$) and also higher than the 2020 target set by the U.S. Department of Energy (DOE) (0.44 A mg$_{Pt}^{-1}$ at 0.9 V, highlighted by a dashed line in Fig. 5c). As shown in Fig. 5d, PtCuAu-8 M shows outstanding specific and mass activities, which suggests a significantly improved kinetics for the ORR. Even when both the mass of Pt and Au are considered, the mass activity of PtCuAu-8 M can still reach 0.97 A mg^{-1} (Fig. S5†). A detailed comparison of the specific surface and mass activities
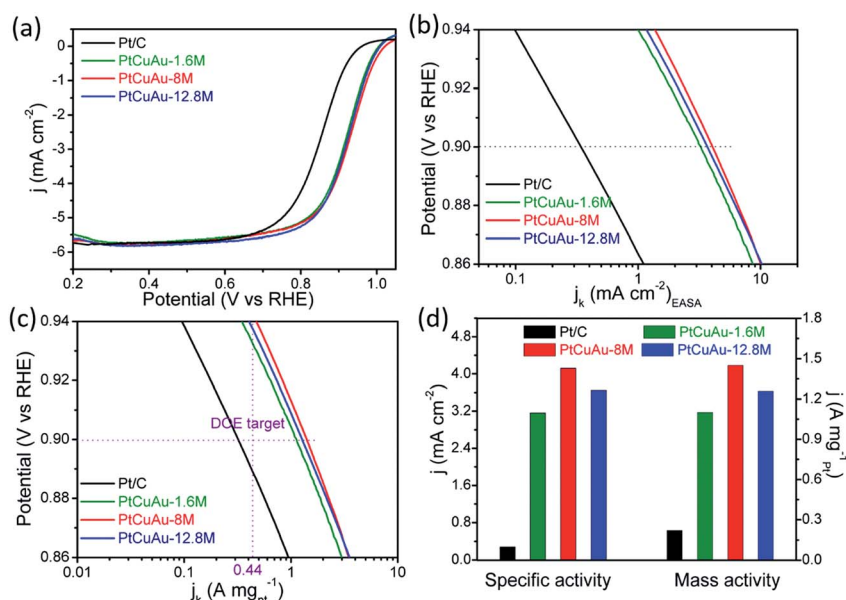

Fig. 5 ORR polarization curves (a), EASA (b) and Pt mass (c) specific Tafel curves, and EASA and Pt mass activities at 0.9 V (d) of the three nanoporous nanowires and Pt/C catalyst in O_2-saturated 0.1 M $HClO_4$, 1600 rpm, and 5 mV s^{-1}.
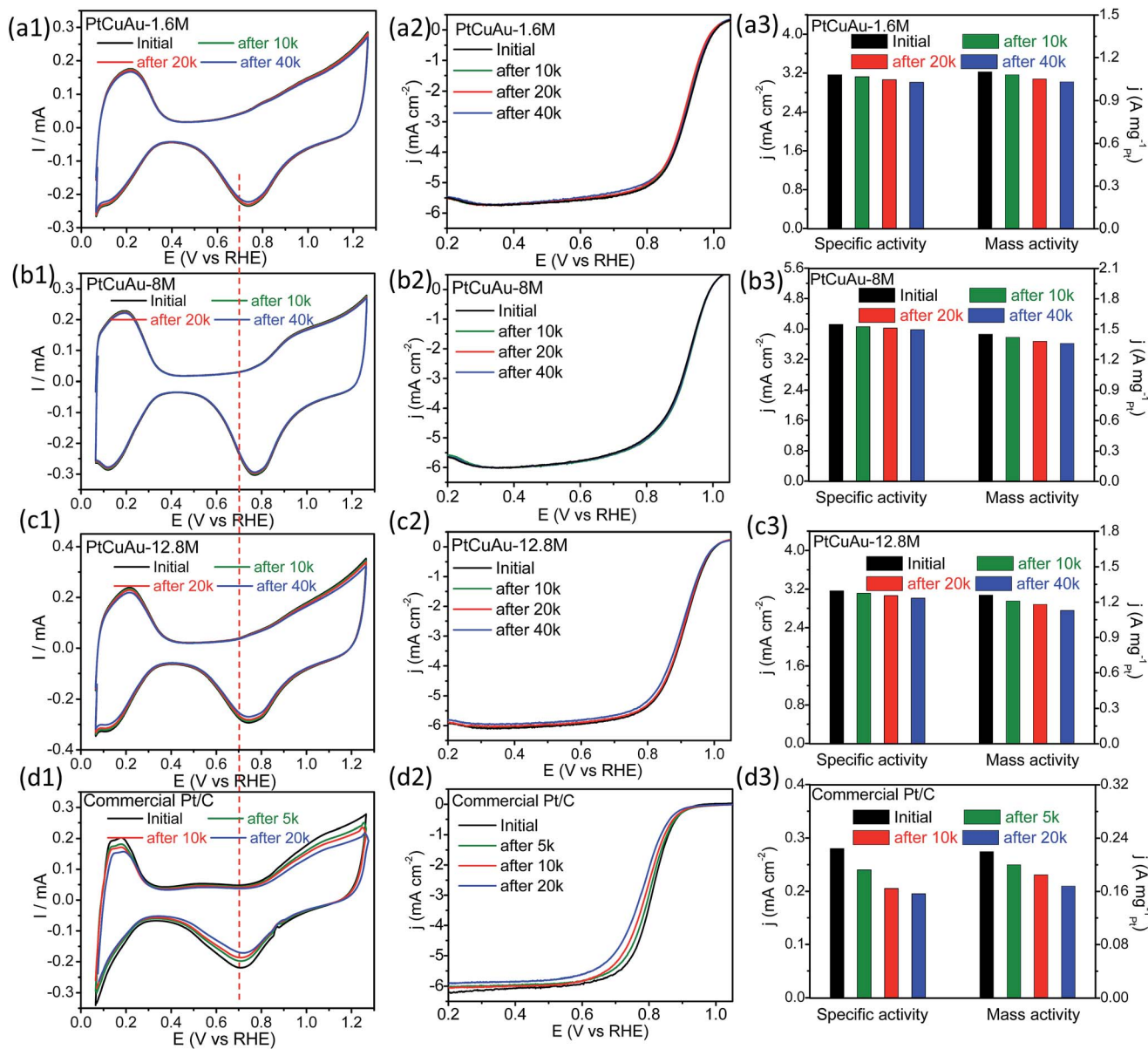
Fig. 6 CV curves (a1, b1, c1 and d1), ORR polarization curves (a2, b2, c2 and d2) and the corresponding histogram of the specific and mass activities of different electrocatalysts before and after different potential cycles (a3, b3, c3 and d3).

of the nanoporous nanowire catalysts with other reported Pt-based nanocatalysts is shown in Table S1.† The activities of the nanoporous nanowires are clearly among the highest values reported.

The durability of the nanoporous nanowires was evaluated using accelerated deterioration tests (ADT) by continuous 40 000 CV cycling from 0.6 to 1.0 V in O_2 saturated 0.1 M $HClO_4$. As shown in Fig. 6b1, the EASAs of the 8 M dealloyed nanowires change negligibly with increasing scan cycles. Even after 40 000 cycles, the EASA and specific activity of the 8 M dealloyed sample dropped by only 3.4%, and the mass activity dropped by only 6.0% (Fig. 6b2 and b3). The EASA, specific activity, and mass activity dropped by 3.7%, 5.1%, and 6.3%, respectively, for the 1.6 M dealloyed sample, and 3.8%, 5.2%, and 10.3%, respectively, for the 12.8 M dealloyed sample (Fig. 6a1–a3 and

c1–c3). In a sharp contrast, the EASA, specific activity, and mass activity of the commercial Pt/C dropped by 34%, 30%, and 35%, respectively, after only 20 000 cycles (Fig. 6d1–d3). This result demonstrates the greatly enhanced durability of the nanoporous ternary nanowires, especially the 8 M dealloyed sample. It is clear that the catalytic performances of the nanoporous nanowires are related to the Cu content. As the Cu content decreases from 45 at% to 37 at%, the ORR activity increases. The activity then decreases slightly when the Cu content further decreases to 27 at%. Strasser and co-workers have shown that the activity of bimetallic Pt–Cu nanoparticles is very sensitive to the surface strain resulting from the lattice mismatch between the Pt-rich shell and the Pt–Cu alloy core.[8,63–68] Thus, the Cu content of 37 at% in this work may provide a suitably strained Pt–Au surface, which delivers the highest activity and

12546 | J. Mater. Chem. A, 2018, 6, 12541–12550

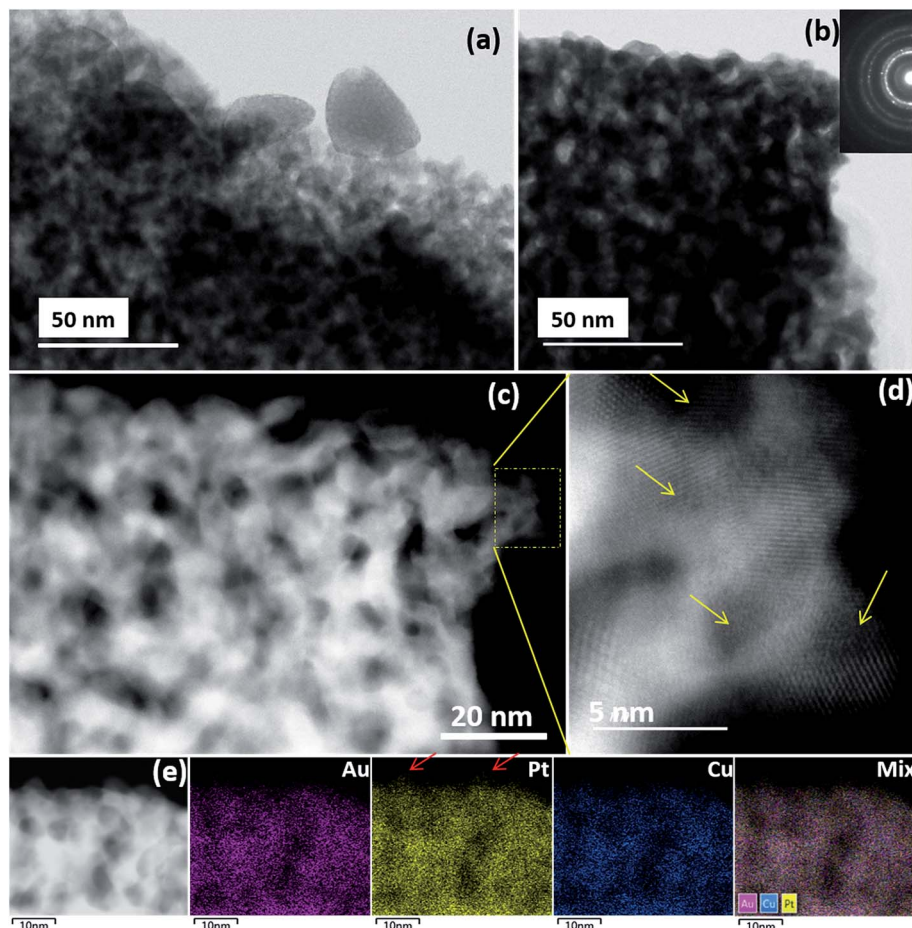This journal is © The Royal Society of Chemistry 2018

Fig. 7 Bright-field STEM images of the nanoporous nanowires. Before (a) and after (b) 40 000 cycles. Inset in (b) is the corresponding SAED image, showing no difference after cycling. HAADF STEM images of the nanoporous nanowires after 40 000 cycles ((c) low magnification; (d) high magnification). The yellow arrows in (d) show some thin parts in the ligament. EDS mapping (e) of the sample after 40 000 cycles. The red arrows in (e) show slight enrichment of Pt on the surface.

durability.[34,35] After the electrochemical durability test, PtCuAu-8 M was further characterized by STEM. Unlike nanoparticulate Pt/C or nanoporous PtNi which will suffer aggregation, coarsening and Ostwald ripening,[69,70] the nanoporous PtCuAu nanowires exhibit no obvious coarsening in the ligaments after 40 000 cycling (Fig. 7b and c). The rugged ligaments with nanoholes and very thin edges are also well preserved (Fig. 7c and d), which is in accordance with the electrochemical CV result in Fig. 6b1, verifying the excellent electrochemical durability of the ternary alloy nanowires. By environmental STEM study, Fujita *et al.* found that in dealloyed nanoporous Au, the subsurface Ag can stabilize surface Au during the CO oxidation reaction.[60] Li *et al.* found that residual Ag played crucial roles in stabilizing the surface active sites and the nanoporous structure during the electrocatalytic oxidation of alcohols.[71] Thus, in this work, the surface Pt step sites should be greatly stabilized by Au and Cu, especially Au which is highly stable even in acidic solutions.[72] EDS mapping reveals that the three elements are still well distributed in the nanowires. Some enrichment of Pt on the out-surface is observed, suggesting the formation of a slightly Pt rich surface. The suitably strained Pt rich surface is clearly beneficial for the electrochemical reactions.

The high catalytic activity and durability of the ternary nanoporous nanowires should also be partly due to the following aspects. Firstly, the inherent ligament-pore structure would provide excellent electron conductivity and also facilitate mass transport during the electrochemical reactions, which can effectively enhance the reaction kinetics.[73] Secondly, the highly exposed (111) planes are the most active Pt plane for the ORR[52] and the high density of surface defect sites (step edges and kinks) would provide more active sites, resulting in greatly enhanced catalytic activity. Thirdly, as demonstrated elsewhere, the uniquely anisotropic nature of 1D nanowires may provide extra structure advantage and/or electronic factors in the catalytic reactions.[74–76]

3. Conclusions

A general and scalable top-down strategy is developed to prepare nanoporous alloy nanowires by controlling the grain size, grain structure, and grain volume shrinkage of a diluted Cu-based bulk precursor alloy. The prepared ternary PtCuAu nanoporous nanowires have relatively uniform and rugged alloy ligaments with highly exposed (111) planes and a high density

This journal is © The Royal Society of Chemistry 2018

J. Mater. Chem. A, 2018, **6**, 12541–12550 | **12547**

of step-edge and kink sites. Moreover, the ternary nanoporous nanowires exhibit greatly enhanced electro-catalytic activity and durability towards the ORR as compared to the commercial Pt/C catalyst due to the structure and composition advantages. This top-down strategy is highly controllable and can be easily extended to fabricate other noble metal/copper-based nanoporous alloy nanowires such as IrCu, RhCu, *etc.*, on a large scale without the use of any organic solvent or surfactant.

4.   Experimental section

Material preparation

The precursor alloy ingots with a composition of $Pt_1Au_{0.5}Cu_{98.5}$ (at%) were prepared by melting pure melts (>99.9 wt%) using an induction-melting furnace under the Ar protection. The precursor alloy was then melted in a quartz tube and injected onto a spinning Cu roller to prepare the alloy ribbons. The tangential speed of the roller is 45 m s^{-1} and the gas pressure for injection is 300 Pa. The thickness of the ribbon is $\sim$20 µm and the width is $\sim$2 mm. Chemical dealloying of the alloy ribbons in a diluted HNO_3 solution was used to prepare the nanoporous nanowires. The catalyst ink for the ORR was made by sonicating a mixture containing a certain amount of nanowires, 4.0 mg carbon powder, 300 µL isopropanol, and 100 µL Nafion (0.5 wt%) for 20 min. The actual loadings of Pt on the glassy carbon electrode were all kept at 10 µg cm^{-2}. The catalyst suspension (4 µL) was coated on a glassy carbon electrode and dried naturally as the working electrode. The Pt/C catalyst (20 wt%, Johnson-Matthey) was used for comparison.

Materials characterization

The samples were characterized using an X-ray diffraction (XRD) diffractometer using Cu Kα radiation (Rigaku D/Max 2500), an X-ray photoelectron spectrometer (XPS, ESCALAB 250), a scanning electron microscope (SEM, HITACHI S-4700) equipped with an energy-dispersive X-ray spectrometer (EDS) and an electron backscattered diffraction (EBSD) detector. EDS was used to determine the compositions of each element in the precursor alloy and dealloyed samples. The local structure and composition were characterized using a JEOL ARM-200F transmission electron microscope (TEM) equipped with a spherical aberration corrector for the probe forming lenses and an EDS detector. The N_2 adsorption/desorption experiment was conducted at 77 K using a Quantachrome Autosorb-3B surface analyzer.

Electrocatalytic oxygen reduction

The electrochemical ORR was carried out on an electrochemical workstation (CHI 660e). A three-electrode system was used including a nanowire-modified glassy carbon rotating disk electrode (diameter: 5 mm) as the working electrode, a Pt wire as the counter electrode, and Ag/AgCl as the reference electrode. The 0.1 M $HClO_4$ electrolyte solution was bubbled with high-purity O_2 for $\sim$30 min prior to the ORR measurements. The scan rate is 5 mV s^{-1} and the rotation rate is 1600 rpm. The electrochemically active surface area (EASA) of Pt was calculated

by considering the charges associated with hydrogen adsorption (0 and 0.3 V) and according to the literature, a monolayer of hydrogen on a crystalline Pt surface is 210 µC cm^{-2}.

Conflicts of interest

There are no conflicts to declare.

Acknowledgements

References

1 V. R. Stamenkovic, B. S. Mun, K. J. J. Mayrhofer, P. N. Ross and N. M. Markovic, *J. Am. Chem. Soc.*, 2006, **128**, 8813–8819.

2 L. Wang and Y. Yamauchi, *J. Am. Chem. Soc.*, 2013, **135**, 16762–16765.

3 S. Guo, S. Zhang, D. Su and S. Sun, *J. Am. Chem. Soc.*, 2013, **135**, 13879–13884.

4 Y. Kang, J. B. Pyo, X. Ye, T. R. Gordon and C. B. Murray, *ACS Nano*, 2012, **6**, 5642–5647.

5 C. Chen, Y. Kang, Z. Huo, Z. Zhu, W. Huang, H. L. Xin, J. D. Snyder, D. Li, J. A. Herron, M. Mavrikakis, M. Chi, K. L. More, Y. Li, N. M. Markovic, G. A. Somorjai, P. Yang and V. R. Stamenkovic, *Science*, 2014, **343**, 1339–1343.

6 J. Wu, A. Gross and H. Yang, *Nano Lett.*, 2011, **11**, 798–802.

7 A.-X. Yin, X.-Q. Min, Y.-W. Zhang and C.-H. Yan, *J. Am. Chem. Soc.*, 2011, **133**, 3816–3819.

8 P. Strasser, S. Koh, T. Anniyev, J. Greeley, K. More, C. F. Yu, Z. C. Liu, S. Kaya, D. Nordlund, H. Ogasawara, M. F. Toney and A. Nilsson, *Nat. Chem.*, 2010, **2**, 454–460.

9 X. L. Tian, Y. Y. Xu, W. Y. Zhang, T. Wu, B. Y. Xia and X. Wang, *ACS Energy Lett.*, 2017, **2**, 2035–2043.

10 X. Ge, L. Chen, J. Kang, T. Fujita, A. Hirata, W. Zhang, J. Jiang and M. Chen, *Adv. Funct. Mater.*, 2013, **23**, 4156–4162.

11 X.-Y. Lang, G.-F. Han, B.-B. Xiao, L. Gu, Z.-Z. Yang, Z. Wen, Y.-F. Zhu, M. Zhao, J.-C. Li and Q. Jiang, *Adv. Funct. Mater.*, 2015, **25**, 230–237.

12 J. Snyder, K. Livi and J. Erlebacher, *Adv. Funct. Mater.*, 2013, **23**, 5494–5501.

13 R. Y. Wang, D. C. Higgins, S. Prabhudev, D. U. Lee, J. Y. Choi, M. A. Hoque, G. A. Botton and Z. W. Chen, *J. Mater. Chem. A*, 2015, **3**, 12663–12671.

14 N. Becknell, Y. Son, D. Kim, D. Li, Y. Yu, Z. Niu, T. Lei, B. T. Sneed, K. L. More, N. M. Markovic, V. R. Stamenkovic and P. Yang, *J. Am. Chem. Soc.*, 2017, **139**, 11678–11681.

15 C. Wang, M. Chi, D. Li, D. Strmcnik, D. van der Vliet, G. Wang, V. Komanicky, K.-C. Chang, A. P. Paulikas, D. Tripkovic, J. Pearson, K. L. More, N. M. Markovic and V. R. Stamenkovic, *J. Am. Chem. Soc.*, 2011, **133**, 14396–14403.

16 Y. Wang, K. B. Yin, J. Zhang, C. H. Si, X. T. Chen, L. F. Lv, W. S. Ma, H. Gao and Z. H. Zhang, *J. Mater. Chem. A*, 2016, **4**, 14657–14668.

12548 | *J. Mater. Chem. A*, 2018, **6**, 12541–12550

This journal is © The Royal Society of Chemistry 2018

17 C. Wang, D. van der Vliet, K. L. More, N. J. Zaluzec, S. Peng, S. H. Sun, H. Daimon, G. F. Wang, J. Greeley, J. Pearson, A. P. Paulikas, G. Karapetrov, D. Strmcnik, N. M. Markovic and V. R. Stamenkovic, *Nano Lett.*, 2011, **11**, 919–926.

18 Z. M. Cui, H. Chen, W. D. Zhou, M. T. Zhao and F. J. DiSalvo, *Chem. Mater.*, 2015, **27**, 7538–7545.

19 T. Y. Jeon, S. K. Kim, N. Pinna, A. Sharma, J. Park, S. Y. Lee, H. C. Lee, S. W. Kang, H. K. Lee and H. H. Lee, *Chem. Mater.*, 2016, **28**, 1879–1887.

20 R. Z. Yang, J. Leisch, P. Strasser and M. F. Toney, *Chem. Mater.*, 2010, **22**, 4712–4720.

21 L. Z. Bu, Q. Shao, E. Bin, J. Guo, J. L. Yao and X. Q. Huang, *J. Am. Chem. Soc.*, 2017, **139**, 9576–9582.

22 L. Z. Bu, N. Zhang, S. J. Guo, X. Zhang, J. Li, J. L. Yao, T. Wu, G. Lu, J. Y. Ma, D. Su and X. Q. Huang, *Science*, 2016, **354**, 1410–1414.

23 H. Y. Kim, S. Cho, Y. J. Sa, S. M. Hwang, G. G. Park, T. J. Shin, H. Y. Jeong, S. D. Yim and S. H. Joo, *Small*, 2016, **12**, 5347–5353.

24 Y. Wang, K. B. Yin, L. F. Lv, T. Y. Kou, C. Zhang, J. Zhang, H. Gao and Z. H. Zhang, *J. Mater. Chem. A*, 2017, **5**, 23651–23661.

25 J. Zhang, K. Sasaki, E. Sutter and R. R. Adzic, *Science*, 2007, **315**, 220–222.

26 M. Gatalo, P. Jovanovic, G. Polymeros, J. P. Grote, A. Pavlisic, F. Ruiz-Zepeda, V. S. Selih, M. Sala, S. Hocevar, M. Bele, K. J. J. Mayrhofer, N. Hodnik and M. Gaberscek, *ACS Catal.*, 2016, **6**, 1630–1634.

27 G. Selvarani, S. V. Selvaganesh, S. Krishnamurthy, G. V. M. Kiruthika, P. Sridhar, S. Pitchumani and A. K. Shukla, *J. Phys. Chem. C*, 2009, **113**, 7461–7468.

28 Y. J. Deng, V. Tripkovic, J. Rossmeisl and M. Arenz, *ACS Catal.*, 2016, **6**, 671–676.

29 M. H. Shao, A. Peles and J. Odell, *J. Phys. Chem. C*, 2014, **118**, 18505–18509.

30 J. B. Wu and H. Yang, *Acc. Chem. Res.*, 2013, **46**, 1848–1857.

31 J. Park, M. K. Kabiraz, H. Kwon, S. Park, H. Baik, S. I. Choi and K. Lee, *ACS Nano*, 2017, **11**, 10844–10851.

32 B. Y. Xia, H. B. Wu, X. Wang and X. W. Lou, *J. Am. Chem. Soc.*, 2012, **134**, 13934–13937.

33 Z. C. Zhang, Z. M. Luo, B. Chen, C. Wei, L. Zhao, J. Z. Chen, X. Zhang, Z. C. Lai, Z. X. Fan, C. L. Tan, M. T. Zhao, Q. P. Lu, B. Li, Y. Zong, C. C. Yan, G. X. Wang, Z. J. C. Xu and H. Zhang, *Adv. Mater.*, 2016, **28**, 8712–8717.

34 L. M. Lyu, Y. C. Kao, D. A. Cullen, B. T. Sneed, Y. C. Chuang and C. H. Kuo, *Chem. Mater.*, 2017, **29**, 5681–5692.

35 L. Zhang, L. T. Roling, X. Wang, M. Vara, M. F. Chi, J. Y. Liu, S. I. Choi, J. Park, J. A. Herron, Z. X. Xie, M. Mavrikakis and Y. N. Xia, *Science*, 2015, **349**, 412–416.

36 H. H. Li, M. L. Xie, C. H. Cui, D. He, M. Gong, J. Jiang, Y. R. Zheng, G. Chen, Y. Lei and S. H. Yu, *Chem. Mater.*, 2016, **28**, 8890–8898.

37 B. Y. Xia, H. B. Wu, Y. Yan, X. W. Lou and X. Wang, *J. Am. Chem. Soc.*, 2013, **135**, 9480–9485.

38 M. F. Li, Z. P. Zhao, T. Cheng, A. Fortunelli, C. Y. Chen, R. Yu, Q. H. Zhang, L. Gu, B. V. Merinov, Z. Y. Lin, E. B. Zhu, T. Yu, Q. Y. Jia, J. H. Guo, L. Zhang, W. A. Goddard, Y. Huang and X. F. Duan, *Science*, 2016, **354**, 1414–1419.

39 C. Z. Zhu, D. Du, A. Eychmuller and Y. H. Lin, *Chem. Rev.*, 2015, **115**, 8896–8943.

40 Q. R. Shi, C. Z. Zhu, Y. J. Li, H. B. Xia, M. H. Engelhard, S. F. Fu, D. Du and Y. H. Lin, *Chem. Mater.*, 2016, **28**, 7928–7934.

41 T. Kwon, M. Jun, H. Y. Kim, A. Oh, J. Park, H. Baik, S. H. Joo and K. Lee, *Adv. Funct. Mater.*, 2018, 1706440.

42 B. K. Pilapil, J. van Drunen, Y. Makonnen, D. Beauchemin, G. Jerkiewicz and B. D. Gates, *Adv. Funct. Mater.*, 2017, **27**, 1703171.

43 Y. Q. Li, C. L. Li, B. P. Bastakoti, J. Tang, B. Jiang, J. Kim, M. Shahabuddin, Y. Bando, J. H. Kim and Y. Yamauchi, *J. Mater. Chem. A*, 2016, **4**, 9169–9176.

44 H. Wang, S. Yin, Y. Xu, X. Li, A. A. Alshehri, Y. Yamauchi, H. Xue, Y. Kaneti and L. Wang, *J. Mater. Chem. A*, 2018, **6**, 8662–8668.

45 S. W. Chou, J. J. Shyue, C. H. Chien, C. C. Chen, Y. Y. Chen and P. T. Chou, *Chem. Mater.*, 2012, **24**, 2527–2533.

46 H. B. Liao and Y. L. Hou, *Chem. Mater.*, 2013, **25**, 457–465.

47 A. Chauvin, C. Delacôte, L. Molina-Luna, M. Duerrschnabel, M. Boujtita, D. Thiry, K. Du, J. Ding, C.-H. Choi, P.-Y. Tessier and A.-A. El Mel, *ACS Appl. Mater. Interfaces*, 2016, **8**, 6611–6620.

48 D. A. Gilbert, E. C. Burks, S. V. Ushakov, P. Abellan, I. Arslan, T. E. Felter, A. Navrotsky and K. Liu, *Chem. Mater.*, 2017, **29**, 9814–9818.

49 L. Liu, E. Pippel, R. Scholz and U. Gösele, *Nano Lett.*, 2009, **9**, 4352–4358.

50 J. Wu and H. Yang, *Acc. Chem. Res.*, 2013, **46**, 1848–1857.

51 D. Wang and Y. Li, *Adv. Mater.*, 2011, **23**, 1044–1060.

52 A. C. Chen and P. Holt-Hindle, *Chem. Rev.*, 2010, **110**, 3767–3804.

53 H. J. Qiu, H. T. Xu, X. Li, J. Q. Wang and Y. Wang, *J. Mater. Chem. A*, 2015, **3**, 7939–7944.

54 C. X. Xu, Q. Hao and H. M. Duan, *J. Mater. Chem. A*, 2014, **2**, 8875–8880.

55 X. Li, Q. Chen, I. McCue, J. Snyder, P. Crozier, J. Erlebacher and K. Sieradzki, *Nano Lett.*, 2014, **14**, 2569–2577.

56 J. Snyder, I. McCue, K. Livi and J. Erlebacher, *J. Am. Chem. Soc.*, 2012, **134**, 8633–8645.

57 W. Luc and F. Jiao, *ACS Catal.*, 2017, **7**, 5856–5861.

58 H. J. Qiu, L. Peng, X. Li, H. T. Xu and Y. Wang, *Corros. Sci.*, 2015, **92**, 16–31.

59 H. J. Qiu, X. Shen, J. Q. Wang, A. Hirata, T. Fujita, Y. Wang and M. W. Chen, *ACS Catal.*, 2015, **5**, 3779–3785.

60 T. Fujita, P. F. Guan, K. McKenna, X. Y. Lang, A. Hirata, L. Zhang, T. Tokunaga, S. Arai, Y. Yamamoto, N. Tanaka, Y. Ishikawa, N. Asao, Y. Yamamoto, J. Erlebacher and M. W. Chen, *Nat. Mater.*, 2012, **11**, 775–780.

61 J. H. K. Pfisterer, Y. C. Liang, O. Schneider and A. S. Bandarenka, *Nature*, 2017, **549**, 74–77.

62 K. Z. Jiang, P. T. Wang, S. J. Guo, X. Zhang, X. Shen, G. Lu, D. Su and X. Q. Huang, *Angew. Chem., Int. Ed.*, 2016, **55**, 9030–9035.

63 V. R. Stamenkovic, B. Fowler, B. S. Mun, G. F. Wang, P. N. Ross, C. A. Lucas and N. M. Markovic, *Science*, 2007, **315**, 493–497.

This journal is © The Royal Society of Chemistry 2018

J. Mater. Chem. A, 2018, **6**, 12541–12550 | **12549**

64 I. E. L. Stephens, A. S. Bondarenko, F. J. Perez-Alonso, F. Calle-Vallejo, L. Bech, T. P. Johansson, A. K. Jepsen, R. Frydendal, B. P. Knudsen, J. Rossmeisl and I. Chorkendorff, *J. Am. Chem. Soc.*, 2011, **133**, 5485–5491.

65 M. Oezaslan, M. Heggen and P. Strasser, *J. Am. Chem. Soc.*, 2012, **134**, 514–524.

66 I. Dutta, M. K. Carpenter, M. P. Balogh, J. M. Ziegelbauer, T. E. Moylan, M. H. Atwan and N. P. Irish, *J. Phys. Chem. C*, 2010, **114**, 16309–16320.

67 J. X. Wang, C. Ma, Y. Choi, D. Su, Y. Zhu, P. Liu, R. Si, M. B. Vukmirovic, Y. Zhang and R. R. Adzic, *J. Am. Chem. Soc.*, 2011, **133**, 13551–13557.

68 C.-H. Cui, H.-H. Li, X.-J. Liu, M.-R. Gao and S.-H. Yu, *ACS Catal.*, 2012, **2**, 916–924.

69 Y. W. Li, J. L. Hart, M. L. Taheri and J. D. Snyder, *ACS Catal.*, 2017, **7**, 7995–8005.

70 R. Y. Wang, C. X. Xu, X. X. Bi and Y. Ding, *Energy Environ. Sci.*, 2012, **5**, 5281–5286.

71 G. G. Li, Y. Lin and H. Wang, *Nano Lett.*, 2016, **16**, 7248–7253.

72 K. Kodama, R. Jinnouchi, N. Takahashi, H. Murata and Y. Morimoto, *J. Am. Chem. Soc.*, 2016, **138**, 4194–4200.

73 P. K. Chen, N. C. Lai, C. H. Ho, Y. W. Hu, J. F. Lee and C. M. Yang, *Chem. Mater.*, 2013, **25**, 4269–4277.

74 C. Koenigsmann, E. Sutter, T. A. Chiesa, R. R. Adzic and S. S. Wong, *Nano Lett.*, 2012, **12**, 2013–2020.

75 C. Koenigsmann and S. S. Wong, *Energy Environ. Sci.*, 2011, **4**, 1161–1176.

76 W. Wang, F. Lv, B. Lei, S. Wan, M. C. Luo and S. J. Guo, *Adv. Mater.*, 2016, **28**, 10117–10141.